A Neural Networks–Based Fusion Technique to Estimate Half-Hourly Rainfall Estimates at 0.1° Resolution from Satellite Passive Microwave and Infrared Data

Francisco J. Tapiador and Chris Kidd

School of Geography, Earth and Environmental Sciences, University of Birmingham, Birmingham, United Kingdom

Vincenzo Levizzani

Institute of Atmospheric Sciences and Climate, National Research Council, Bologna, Italy

Frank S. Marzano

Department of Electric Engineering, University of L'Aquila, L'Aquila, Italy

(Manuscript received 14 August 2002, in final form 14 September 2003)

ABSTRACT

The purpose of this paper is to evaluate a new operational procedure to produce half-hourly rainfall estimates at 0.1° spatial resolution. Rainfall is estimated using a neural networks (NN)–based approach utilizing passive microwave (PMW) and infrared satellite measurements. Several neural networks are tested, from multilayer perceptron to adaptive resonance theory architectures. The NN analytical selection process is explained. Half-hourly rain gauge data over Andalusia, Spain, are used for validation purposes. Several interpolation procedures are tested to transform point to areal measurements, including the maximum entropy estimation method. Rainfall estimations are also compared with Geostationary Operational Environmental Satellite precipitation index and histogram-matching results. Half-hourly rainfall estimates give ~0.6 correlations with PMW data (~0.2 with gauge), and average correlations of up to 0.7 and 0.6 are obtained for 0.5° and 0.1° monthly accumulated estimates, respectively.

1. Introduction

The importance of rainfall estimation in weather forecasting, hydrological models, and hazard monitoring and assessment is growing. Furthermore, rainfall monitoring is also important for agriculture, fisheries, famine early warning, pest monitoring, and erosion processes. While some of these applications can use gauge observations, others such as weather forecasting need more comprehensive coverage. In addition, there is a major need for short-period estimates (Vicente et al. 1998). Applications such as numerical forecasting require appropriate and timely rainfall measurements for data assimilation. Moreover, knowledge about rainfall processes can also be increased if large-scale, more continuous rainfall series are available. Increasing spatial resolution is also desirable for applications such as agriculture (Herman et al. 1997) or hazard monitoring, which require a resolution below the basin level. Improvements to hydrological model forecasts are possible

with inputs that minimize sampling frequency errors. However, these requirements are not completely met using rain gauge stations alone and can only be realistically provided by spaceborne sensors.

Satellite rainfall retrievals have many advantages over rain gauge–based measurements. The most obvious one is the spatial coverage, especially over the oceans where rainfall measurements are sparse. Temporal sampling capabilities for large areas is also a major difference: only timely satellite estimates permit the development of real time or near-real-time applications. Satellite data are also more homogeneous and objective than rain gauge data.

However, current satellite rainfall retrievals are limited by two factors. First, passive microwave (PMW)-based estimates suffer from poor temporal sampling and coarse spatial resolution but determine rainfall more directly. Infrared (IR)-based sensors provide better temporal resolution and moderate spatial resolution but determine rainfall indirectly by inference from cloud-top temperatures. Data fusion procedures aim to combine both datasets to generate a product without their limitations while reinforcing their strengths (e.g., Turk et al. 1999; Marzano et al. 2002).

Corresponding author address: Dr. Francisco J. Tapiador, School of Geography, Earth and Environmental Sci., University of Birmingham, B15 2TT Birmingham, United Kingdom.
E-mail: f.tapiador@bham.ac.uk

Combined PMW and IR algorithms have been developed in the past, many of which represent developments of the Geostationary Operational Environmental Satellite (GOES) precipitation index (GPI). Adler et al. (1993) developed the adjusted GPI (AGPI), in which a correction factor is derived from comparison of PMW and GPI estimates for coincident time slots over some extended period (typically 1 month). This correction is then retrospectively applied to all the GPI estimates during that period. Kummerow and Giglio (1995) and Xu et al. (1999) have subsequently developed more sophisticated approaches such as the universally adjusted GPI (UAGPI) method, which is optimized using coincident PMW and IR data, again over an extended period. Anagnostou et al. (1999) show a PMW-calibrated IR method for regional-scale applications while Todd et al. (2001) present a new combined PMW and IR satellite algorithm (MIRA) for estimation of rainfall at the smallest possible space and time scales. It is based on the assumption that PMW algorithms can provide accurate estimates of instantaneous rain rates and that this information can be used to calibrate IR parameters to improve rainfall estimates from IR data that are available at high temporal frequency.

This paper presents a neural networks (NN)–based data fusion working procedure and tests its performance through comparison with other more conventional techniques such as the GOES precipitation index and a histogram-matching (HM) technique. The present method differs from previous NN work such as proposed by Sorooshian et al. (2000) and Bellerby et al. (2000) since instantaneous rather than accumulated rainfall is the desired product. Although validation procedures require calculated monthly accumulated values, the goal is to generate actual instantaneous (30 min) estimates at a better spatial resolution than current techniques. The study also uses PMW data from the Special Sensor Microwave Imager (SSM/I) rather than other tropical-oriented sensors such as the precipitation radar (PR) of the Tropical Rainfall Measuring Mission (TRMM) used in most of the previous studies. Therefore almost global coverage, including midlatitude areas where the most accurate field validation data can be found, is available.

2. Data analysis

a. Background

1) SATELLITE RAINFALL RETRIEVALS

Two main approaches have been used to obtain satellite rainfall retrievals. Some review articles have analyzed the capabilities and performance of visible/infrared (VIS/IR) algorithms (e.g., Levizzani et al. 2001). However, there is only an indirect relationship between cloud-top temperatures and actual rainfall. VIS/IR-based algorithms seem to work best for large spatial scales or long time series mainly because of a statistical smoothing effect. Another reason is the relationship between cold-cloud duration and long-term measured rainfall for certain climatic typologies. Despite reasonably good correlations, the physics of the rainfall retrieval problem and the dynamics of the frontal systems are overlooked altogether.

Conversely, PMW techniques provide more direct observation of the rainfall since it is the raindrops themselves that modify the upwelling radiation measured by the satellite. Nonprecipitating clouds are almost transparent at frequencies below 40 GHz, but at the same wavelength hydrometeors interfere with the background radiation. Since radiation scattering, absorption, and emission are related to the size and number of raindrops, a direct physical relationship—although complicated and affected by several impairments—can be established. However PMW techniques have poor spatial and temporal resolutions limited by technical requirements of the sensors and their low earth orbit (LEO) platforms. Spatial resolution cannot be improved because of the antenna diffraction limit related to the centimeter wavelength of the radiation itself, and temporal resolution can only be enhanced by using a constellation of satellites in low orbit. On the other hand, VIS/IR images are available at higher spatial and temporal resolutions. New sensors such as the new Meteosat Second-Generation (MSG) Spinning Enhanced Visible and Infrared Imager (SEVIRI) will provide 15-min, 12-band measurements with a resolution at subsatellite point varying from 1.4 (high-resolution VIS) to 4.8 km (IR) (Schmetz et al. 2002).

Data fusion approaches intend to take advantage of the strengths of both data types while avoiding their weaknesses as much as possible. The ultimate goal is to find a more direct measurement of the rainfall than that inferred from IR cloud-top brightness temperatures, while providing a spatial resolution one order of magnitude better than that of the PMW sensors at a much better temporal sampling.

A complete discussion on the advantages and disadvantages of VIS/IR and PMW rainfall retrieval algorithms can be found in Levizzani et al. (2001). PMW algorithms are either statistical–empirical algorithms or physical, radiative transfer equation–model based. Whereas the ultimate goal of rainfall estimation might be to propose a physical model, this task is hindered by two facts. First, because climate is a time-dependent phenomenon, changes must already be known to establish a deterministic physical model. Even more important, the nonlinear behavior of the variables involved prevents a deterministic modeling approach. Despite the importance of microphysical studies some statistical assumptions are required even for small-scale estimates around 1 km. Note that considering statistical methods versus deterministic ones does not mean lack of scientific content. On the contrary, it can be argued that when a large number of particles or variables are involved, the statistical approach is the only viable methodology. Jaynes' arguments on statistical mechanics

(Jaynes 1990) can be effectively applied to the problem of rainfall estimation.

2) RETRIEVAL VALIDATION ISSUES

Results are validated over a Mediterranean region, a climatic scenario substantially different from that of the Tropics since neither the diurnal rainfall cycle nor the precipitation processes are comparable, and the accumulated rainfall amounts are completely different. The lower rainfall rates in the Mediterranean as compared with the convectively active Tropics imply less chance to encompass errors through spatial or temporal averaging. The general dominance of the frontal systems over convective processes represents a challenge for rainfall estimation since the ability to discriminate rainfall areas within satellite imagery is limited by the complexity of the intermixed phenomena (convective and stratiform) and the generally lower rain rates.

Monthly accumulated products are not necessarily superior with respect to instantaneous estimates. On the contrary, a loss of any intermediate data can result in a very biased estimation. For example, while a couple of lost satellite scenes does not represent a problem in the high-rainfall areas of the intertropical convergence zone (ITCZ), these could be precisely the images that reveal the weekly rainfall in a given cell over a lower-rainfall area in the Mediterranean basin. Consequently validation data and satellite imagery used in the fusion algorithms must be as continuous as possible.

A statistically based approach is used to fuse the PMW and IR data so that the strengths of each individual dataset are maintained and their weaknesses are at least partially corrected for (cf. Marzano et al. 1999). The use of gauge data was intended for the validation at several temporal and spatial scales. However, caution must be used while comparing these data. The large spatial variability of the rainfall rates implies that areal estimations from point measurements are difficult to estimate. Interpolation procedures always contain an unrealistic smoothing effect, even if the least possible bias is involved. Moreover, the relationship between rainfall rate and rainfall duration makes it difficult to covert the satellite instantaneous snapshots into accumulated 30-min rainfall. Intensity–duration–frequency (IDF) curves provide only a certain degree of accuracy and should be applied to large time and spatial scales. Therefore the bias associated with the 0–30-min transformation must be considered when the quality of validation results is assessed.

b. Satellite data sources

1) PASSIVE MICROWAVE DATA

Based on the Electronically Scanning Microwave Radiometer (ESMR) aboard *Nimbus-5* and *-6,* spacecraft that compose the Defense Meteorological Satellite Program (DMSP) carry aboard the enhanced SSM/I system. The first DMSP satellite (*F8*) with an SSM/I was launched in 1987. The latest DMSP spacecraft (*F15*) was launched in December 1999 and became operational in February 2000. The SSM/I sensor measures the earth's microwave emission and has a near-circular, sun-synchronous, near-polar orbit at an altitude of 860 km with an inclination of 98.8° and an orbital period of 102 min. This provides complete coverage of the earth, excluding two 2.4° circular sectors centered on the Poles. Spatial sampling resolution is 12.5 km pixel^{-1} at 85 GHz and 25 km pixel^{-1} at the lower frequencies. Calibration is done once each sensor scan (period 1.899 s) with a cold (3.1 K) and a warm (300 K) target. SSM/I data are obtained from the National Aeronautics and Space Administration's (NASA) Marshall Space Flight Center (MSFC).

Many rainfall-rate retrieval algorithms have been proposed (cf. Ferraro 1997; Smith et al. 1998). Here, a frequency difference algorithm described in (Ebert 1996) is used. Its physical basis is that the 85-GHz channel will be more greatly affected than the lower-frequency, 19-GHz channel because of scattering from precipitation-sized particles. Rain rates (RR) are generated through a lookup table derived from coincident measurements with TRMM PR. This empirical method aims to minimize the effects of surface temperature, emissivity, and atmospheric effects. Vertical polarization channels are used over the ocean, with the horizontal polarization used over land areas. Estimates over coastal regions are produced by a polarization-corrected temperature algorithm (see Kidd 1998).

2) INFRARED DATA

Since the VIS images cannot be properly used during nighttime, only IR can provide a complete daily series. Globally merged, full-resolution (~4 km), radiometrically corrected IR data from the Climate Prediction Center/National Centers for Environmental Prediction (NCEP)/National Weather Service (NWS) are used. These data are formed from the ~11-μm IR channels aboard the *Geostationary Meteorological Satellite-5* (*GMS-5*), *GOES-8, GOES-10, Meteosat-7,* and *Meteosat-5* geostationary satellites. Details are provided by Janowiak et al. (2001). Global images are resampled to 0.036° resolution for the area of interest. This merged product and the location of the area in the Meteosat domain ensures a valid image every 30 min.

c. Ancillary ground data

1) RAIN GAUGE DATA

Gauge data were provided by the 89 agro-meteorological stations of the European Union (EU) Regional Government of Andalusia, Spain. Figure 1 shows the validation area with the spatial distribution of rain gauge
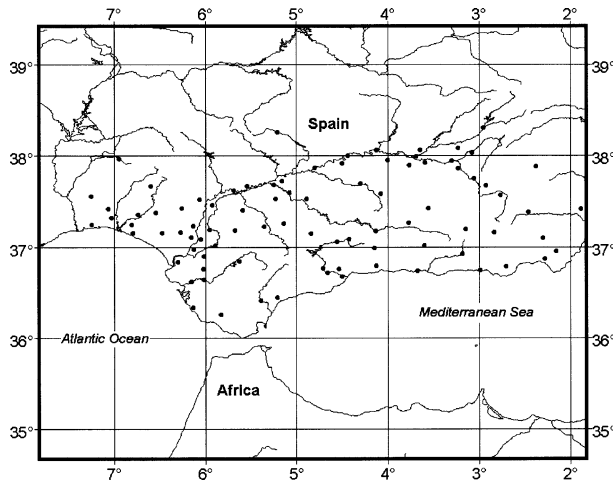
FIG. 1. Validation area showing the hydrographical net, political boundaries, and the 89 gauge stations used for satellite validation.

data. Both the area covered (35°–39°N, 7.5°–1.5°W) and the 30-min temporal sampling of the measurements are deemed appropriate for validation purposes.

The interest in this region is twofold. First, the available data, which come from automatic stations, are quality controlled through preprocessing and comparison with independent measurements from the national rain gauge network. Complete station series may be omitted if deemed unreliable, thus ensuring the best possible reliability of the measured values. The second reason of interest is the location of the region, allowing a different kind of comparison than those available from past PMW validation campaigns such as TRMM's, operating in areas where the diurnal cycle is pronounced. The Andalusia climate can be summarized as Mediterranean: The average annual temperature is 16.8°C, while rainfall is 630 mm. However, the rainfall oscillation is pronounced: from 200 to 2000 mm with very variable instantaneous rainfall rates. From a physical point of view, the region can be divided into three main sectors: 1) the mountain areas including the Sierra Nevada (SE), with elevations up to 3478 m, and the Sierra de Grazalema-Ronda; 2) the Gualdalquivir river valley crossing the region SW–NE, and 3) the plains in the east. Each of these areas presents very different rainfall regimes with peak rainfall amounts in the SE.

2) SPATIAL INTERPOLATION PROCEDURES

Several interpolation methods were applied to the rain gauge point data to derive areal estimates. For cumulative values several methods have been proposed (e.g., Sivapalan and Blöschl 1998). Instantaneous values are usually estimated through interpolation procedures as described in a special issue of the *Journal of Geographic Information and Decision Analysis* (1998, Vol. 2, no. 1–2). Distance weight-averaged, bilinear and quadratic interpolation, various kriging

models, and maximum entropy interpolation are compared in the search of the least-biased method, using different grid intervals. Eventually, maximum entropy interpolation method is used for 0.1° and 0.5° interpolations.

The maximum entropy method (MEM) was developed by Jaynes (Jaynes 1963, 1990). His Shannon's-based definition of information entropy (Shannon 1948) provides a criterion for setting up probability distributions without spurious assumptions. Epistemologically, the MEM presents some advantages in science, as has been reinforced by many researchers (in particular Shore and Johnson 1980). This method has been widely applied in physics, as when reconstructing the major concepts of the classical statistical mechanics from a purely Shannon information definition start. Several methods have been derived from Jaynes' ingenious findings and have been applied in signal processing (Skilling and Bryan 1984), image restoration (Noll 1997), and satellite imagery data fusion (Tapiador and Casanova 2002). Christakos (1991) presented a method to apply the formalism in geospatial interpolation. This procedure is followed here in the Lee and Ellis (1997) development.

The MEM provides an objective procedure to find the least-biased probabilistic distribution of a univariate or multivariate random function. It can be demonstrated that this distribution extracts the maximum knowledge out of the problem (maximum entropy principle). The formalism is as follows. The information contained in a probabilistic distribution or random variable $\mathbf{R}(x, y)$ is consistently measured by their entropy function:

$$S[\mathbf{R}(x, y)] = -\sum_{i=1}^{m} \sum_{j=1}^{n} \mathbf{R}(x_i, y_j) \log\mathbf{R}(x_i, y_j). \quad (1)$$

The MEM states that the most unbiased probabilistic distribution yields from the maximization of S subject to the set of $r + 1$ constraints:

$$1) \qquad \sum_{i=1}^{m} \sum_{j=1}^{n} \mathbf{R}(x_i, y_j) = 1 \quad \text{and} \qquad (2)$$

$$2) \quad \sum_{i=1}^{m} \sum_{j=1}^{n} \mathbf{R}(x_i, y_j)g_k(x_i, y_j) = \overline{c_k} \quad k = 1, \ldots, r, \qquad (3)$$

where $g_k(x, y)$ are linear moments with respect to the $\mathbf{R}(x, y)$ vector with expected values $\overline{c_k}$. We apply here the discrete formalism without loss of generality. However, some discussion remains on the continuous formalism general-case theoretical base.

To maximize the entropy S subject to the constraints, a variational approach is normally used, solving the

system through Lagrangian multipliers. In its simplest, nontrivial two-constraints form,

$$L[\mathbf{R}(x,\ y),\ \lambda_1,\ \lambda_2]$$

$$= -\sum_{i=1}^{m}\sum_{j=1}^{n}\mathbf{R}(x_i,\ y_j)\ \log\mathbf{R}(x_i,\ y_j)$$

$$+ \lambda_1\left\{\left[\sum_{i=1}^{m}\sum_{j=1}^{n}\mathbf{R}(x_i,\ y_j)\right] - 1\right\}$$

$$+ \lambda_2\left\{\left[\sum_{i=1}^{m}\sum_{j=1}^{n}\mathbf{R}(x_i,\ y_j)g_k(x_i,\ y_j)\right] - \overline{c_1}\right\}. \quad (4)$$

Then solving (for x) yields

$$\frac{\partial L}{\partial f(x_i)} = -[\log\mathbf{R}(x_i) + 1] + \lambda_1 + \lambda_2\overline{c_1} = 0. \quad (5)$$

This results in a nonlinear system of equations that must be solved by numerical methods. Alternatively, a dual problem can be defined minimizing the a posteriori uncertainty through a maximum entropy estimate $\overline{z}^*$. After some calculations, the necessary condition for a minimum results

$$\left.\frac{d\ \log[\mathbf{R}(z,\ x,\ y)]}{dz}\right|_{z=\overline{z}^*} = 0. \quad (6)$$

Because the Shannon's information function is convex, this condition is also sufficient. In the general case, this results in a set of equations that need to be solved through numerical methods. Nevertheless, if the prior information (the constraints) consists of the two first moments of the distribution, the joint distribution characterized by the maximum entropy principle is then Gaussian, as was shown by Kapur and Kesavan (1992). Thus

$$\mathbf{f}(z,\ x,\ y) = \frac{1}{[(2\pi)^{n-1}|\mathbf{\Sigma}|]^{1/2}}$$

$$\times \exp\left[-\frac{1}{2}\sum_{i=1}^{m}\sum_{j=1}^{n}a_{ij}\frac{(x_i - \mu_i)}{\sigma_i}\frac{(y_j - \mu_j)}{\sigma_j}\right] \quad (7)$$

with $\mathbf{\Sigma}$ the covariance matrix and a_{ij} the ijth value of the $\mathbf{\Sigma}^{-1}$ matrix (Lee and Ellis 1997). This allows a practical implementation of the MEM. Equation (6) is then solved, which yields

$$\overline{z}^* = m_1 - \frac{\sigma_1^2}{a_{11}}\sum_{i=1}^{n}a_{i1}\frac{[\mathbf{R}(x_i,\ y_i) - \mu_i]}{\sigma_1\sigma_i}. \quad (8)$$

This can then be calculated easily using a simple kriging algorithm (Lee 1998). It can be proved that the second moments are also equivalent. Empirical tests between the actual calculation of the MEM and this approach result in high correlation values (>0.99).

3. Fusion techniques

a. Neural network method

The NN nonparametric approach presents many advantages over other statistical procedures (Sarle 1994). Hornik et al. (1989) have proved that multilayer perceptron NN can approximate any measurable function up to an arbitrary degree or accuracy. As a semiparametric regression estimator, NNs can model a nonlinear function in a finite number of steps. Moreover, most of the classification statistical procedures can be taken as particular cases of NNs. This ability to extract nonlinear relationships is a very valuable feature in remote sensing. At least in theory, NNs can improve classification accuracy by 10%–30% in comparison with conventional classification methods (Carpenter et al. 1997).

Neural networks have been widely used in rainfall estimation, and two main streams can be recognized. First, there is the use of NNs within physical inversion procedures using radiative transfer equations (e.g., Li et al. 1997a,b). Other approaches analyze the problem as a statistical one, as was done by Sorooshian et al. (2000) when presenting a GOES-IR–TRMM Microwave Imager (TMI) working procedure to generate daily estimates with $1° \times 1°$ resolution. Hsu et al. (1999) have worked on approximating the statistical relationships between VIS and IR data and rainfall. Correlations above 0.7 can be generated for monthly totals at $0.5° \times 0.5°$ using several approaches and models. Outliers were in all cases reduced by accumulating samples both spatially and temporally.

1) NEURAL NETWORK MODEL ANALYSIS

Several NN models were tested in the preliminary stage of the present work. The selection of the model was not a blind process but a conscious and analytical quest. Following Anders and Korn (1999), a statistical analysis was performed with the data in order to find the most appropriate structure for the net through hypothesis testing, information criteria, and cross-validation methods. In particular, the information criteria model selection was followed once the most appropriate architecture was chosen, that is, a multilayer perceptron (MLP) NN. Model selection can be guided by previous statistical modeling, which provides a conscious NN architecture selection. The procedure followed here was to use the network information criterion (NIC; Murata et al. 1994) with a previous transfer function linear transformation through Taylor series expansion. NIC is defined as

$$\text{NIC} = -\frac{1}{n}\log L(\hat{w}) + \frac{\text{tr}[\mathbf{BA}^{-1}]}{n} \quad (9)$$

with $\mathbf{A} \equiv -E[\nabla^2 \log L_i]$, $\mathbf{B} \equiv E[\nabla \log L_i \nabla \log L_i']$, n the number of observations, $\hat{w}$ the set of parameters, ∇ the gradient, ∇^2 the Hessian, and log L the estimated maximum log likelihood. This criterion is not justifiable,

however, for overparameterized nets whose limiting distributions are mixed Gaussian. However, a Taylor series expansion of an additional hidden unit transfer function reduces the hidden unit to linear terms and makes it possible to use the NIC.

The method is as follows. First, the number of hidden units is decided. Then, the Taylor expansion for the additional unit and the principal components are calculated and regressed with the residuals of the models. The next step is to calculate the NIC, accepting the additional component if it improves the overall performances. In a second stage, this fully connected net is pruned, extracting subsets and comparing with the NIC estimator again. After this process, Monte Carlo simulations show that the results increase the classification capabilities.

To determine the MLP choice, several models were previously tested. Also, some adaptive resonance theory (ART) nets (Carpenter et al. 1989) were tested because of their fast learning ability. ART1 (adapted to the input dataset), ART2, ARTMAP, distributed ARTMAP, and fuzzy ARTMAP were generated, trained using the 1800 UTC 10 December 2001 SSM/I image and tested with a different SSM/I–IR pair (0630 UTC 10 December 2001).

ART architectures develop the Grossberg (1969) adaptative resonance theory. The idea behind this paradigm is to develop a procedure to solve the false encoding problem, using two fields of neurons. One F^x field acts as ''sensorial cells'' and the other F^y acts as ''high level'' processing units. The inclusion of a ''trigger'' ability to inhibit or disinhibit false patterns represents an improvement over the MLP approach, which is unable to distinguish false patterns that are actually used in the training process. ART nets present good behavior in near-real-time processes. However, this feature is not the major reason for interest in using the ART paradigm in rainfall data fusion—rather it is its ability to identify spatial patterns. This was the primary use of ART models in their original image processing–related applications.

Because of the ART model sensitivity to the order in which the data are presented to the net, a voting procedure is required. Carpenter et al. (1997) themselves acknowledge the need for this additional feature in their model when applied to remote sensing data. It is empirically shown in this study that for one particular case no less than 30 different arrangements were needed to obtain any results.

Several approaches have been described to overcome this problem (Carpenter et al. 1997; Dagher et al. 1999). The algorithm suggested by Dagher et al. (1999) is applied to select the pattern order presentation within a rational framework, reaching stationary values around a large value of 1000 orderings, slowing down the learning process. Nevertheless, this procedure provides a rational, straightforward, easy-to-compute method to present the patterns to the net in the training phase. The

TABLE 1. Statistics for a pixel–pixel comparison (0.1 mm h^{-1}) for the neural networks models evaluated using a sample image (1800 UTC 12 Oct 2001). Spatial resolution is 25 km.

Model	R^2	Avg	Bias	MSE in training
FF MLP	0.95	23.44	4.12	0.018
ART1	0.23	12.37	23.34	0.018
ART2	0.32	11.43	56.12	0.030
ARTMAP	0.25	16.72	12.98	0.027
Fuzzy ARTMAP	0.42	12.12	32.17	0.012
Distributed ARTMAP	0.37	20.43	22.23	0.005
Test image	1.00	22.53	–	–

algorithm consists of four stages. First, for each training pattern $\mathbf{x} = (x_1, \ldots, x_k, x_{k+1}, \ldots, x_n)$,

$$G = \sum_{i=1}^{k} |x_{k+i} - x_i| \qquad (10)$$

is computed. Second, the training pattern that maximizes Eq. (10) (say x_0) to the NN is presented, and then x_0 is removed from the training data. The next c patterns are chosen as follows. The Euclidean distance between x_0 and the training patterns is calculated, and the minimum x_j is selected. This is iterated using $x_0 = x_j$ until $j = c$, where c is the number of classes desired plus one. This generates a set of c I_c cluster centers, whose maximum value is computed. The corresponding training pattern is the next to be presented to the net. Once used, the pattern is removed and the calculation of the cluster centers step iterates.

The third stage consists of the selection for the next $n - c$ parameters computing the Euclidean distance of the remaining patterns to the cluster centers and selecting the minimum of these distance patterns as the next input. Then, the pattern is removed and the process iterated until all the input patterns have been used.

It can be proved that the generated ordering is independent of the one associated with the original training set (Dagher et al. 1999). Experimental work of the authors also proves that the generalization performance is increased. Table 1 shows the results of this selection process. Note that, despite good behavior in the training phase, ART models fail when applied to new patterns.

2) ARCHITECTURE SELECTION

The chosen architecture is a simple MLP feed-forward model with 11 input neurons, 23 and 7 units in two hidden layers, and a unique output neuron. From a mathematical point of view it has been argued that no more than two hidden layers are required for any kind of data, and only one if the function to be modeled is revealed as continuous (Cybenko 1989). However, practical issues such as training speed can suggest other decisions. In this study, after the model selection an empirical test confirms that no further improvement was obtained by increasing the number of hidden layers.

TABLE 2. Inputs used for the neural network model.

Inputs	Notation	Description
1–6	T_b at $t_0, \ldots, t_5$	Brightness temperature of the pixel for the current IR image (t_0) and the previous five images
7	$\overline{T_b} \, (3 \times 3)$	Mean value over a 5 by 5 pixel neighborhood of the current IR image
8	$\overline{T_b} \, (5 \times 5)$	Mean value over a 3 by 3 pixel neighborhood of the current IR
9	$\nabla T_b \, (3 \times 3)$	Standard deviation of pixel value over the 3 by 3 pixel neighborhood image
10	$\nabla T_b \, (5 \times 5)$	Standard deviation of pixel value over the 5 by 5 pixel neighborhood
11	$\#(T_b < 225)$	Number of pixels of current IR image with a brightness temperature less then 225 K

Sigmoidal functions are used in all the neurons but with different parameterizations. Also, a binary output in 100 classes has proved to be worse than the chosen one for increasing the efficiency of the net.

3) INPUTS SELECTION

The inputs of the net have been selected bearing in mind the precipitation processes in the area of study. Only the IR band was used, enabling generation of daytime and nighttime estimates: further research must be done using more IR bands to help in identifying cirrus, cloud, fog, and mist, which are sometimes mistaken for rain areas.

The first six inputs consist of the current and the five previous brightness temperature values for a particular pixel. This is expected to model not only the convective and orographic processes but also the frontal ones in the southern Mediterranean area. Each rainfall process generates a very different signature or sequence of digital numbers in the same pixel, but it was expected that the training process would be able to recognize them when associated with a certain amount of rain and additional spatial information. The next two inputs are the average over a 3×3 and 5×5 neighborhood of the pixel. This minimizes the geolocation and synchrony problems of both datasets. Second, it provides valuable texture information about the cloud cover (Bellerby et al. 2000). Standard deviations of the current value with the 3×3 and 5×5 windows were taken as the next two inputs. Last, the number of pixels whose associated temperature is lower than 225 K in the 3×3 slot was also included. This value is intended to provide information about the heaviest rain areas. A previous empirical test showed that the 225-K threshold was more appropriate to this area than the more usual 235-K value recommended in the literature. This variability of the threshold has been pointed out by several authors. Todd et al. (1995) and Todd and Washington (1999) showed that optimum IR threshold values (calculated by comparison with rain gauges) over East Africa are highly variable in time and space, as a result in local-scale rainfall/cloud characteristics. Such optimized IR threshold fields were shown to identify rainfall events more accurately than a fixed 235-K threshold. Xu et al. (1999) also demonstrated the value of local calibration of IR thresholds (using PMW satellite on a monthly basis) over the Japanese islands.

The time of the day input was considered as invalid early, since the NN can become coupled with the value itself. The reasonable performances of models using this input can be attributable to strong daily rainfall cycles such as in the Tropics where the net could learn the daily convective succession oblivious of the other inputs. Table 2 summarizes the inputs used. The output corresponds to the estimated SSM/I instantaneous rainfall rate (in tenths of millimeters). All absolute values were normalized to [0, 1].

4) OPERATIVE DATA PROCESSING

The procedure followed to generate the 30-min estimates is to train the net with every valid SSM/I overpass. The temporal sampling of these satellites allows typically twice-daily imagery of the area under study. This means that at least two nets are generated, trained, and applied each day, but because of the region's climate this produces various scenarios. In this Mediterranean area, only a single coincident image containing a rainfall pair is usually found over a long period of time. In this case, the closest nets are used to generate the estimates. This represents an additional uncertainty that is reflected in the final results.

The learning rates in the training phase were set to 0.1 for the first 10 000 iterations and to 0.05 for the next 10 000. Several selected cases showed that the mean-square error (MSE) of the net was always less than 0.002 within the 20 000-iterations limit. An independent validation dataset was also employed to ensure the generalization properties of the trained net. The overtraining effect was avoided by using these complementary data.

5) INVERSION PROCEDURE

An inversion procedure was followed to analyze the influence of the inputs on the final result. Input selection cannot be parameterized in the same way as the NN model is. The physics of the problem relies on a rational choice of the factors that can have an a priori relationship with the instantaneous rainfall rate. Nevertheless, once the net is trained some algorithms have been pro-

posed to uncover the almost black-box procedure that the training process represents. The NN inversion procedures seek to find one or more input values that produce a desired output response for a fixed set of synaptic weights (Jensen et al. 1999). The basic idea is to analyze the kind of input vector that generates a specific output. This could be useful both for the input selection process and for the analysis of the process being modeled.

The inversion of neural networks seeks to find the input vector that corresponds with a desired output. Once the training dynamic process has been completed, an NN is nothing but a matrix of weights that best fits the inputs to the outputs. If we consider an NN as a function f that gives a desired output $\mathbf{y}$ from some inputs $\mathbf{x}$,

$$\mathbf{y} = f(\mathbf{x}, \mathbf{W}) = \sum_{i=1}^{H} w_i^h g\left(\sum_{j=0}^{I} w_j^{ih}\right) x_i, \qquad (11)$$

where H and I denote the hidden and input layers, respectively, and g is the transfer function. Once the NN has been trained, the matrix $\mathbf{W}$ becomes fixed. To retrieve an estimated input from a given output o^*, a cost error function must be minimized:

$$\min e(\mathbf{x}) = [f(\mathbf{x}, \mathbf{W}) - o^*]^\alpha. \qquad (12)$$

In general, the solution is a set of k-uple on hypersurfaces, so that there are many solutions to a given output. In some NN applications this can be a problem, but in our case this is in agreement with our hypotheses on rainfall processes.

Several approaches have been proposed to solve the optimization problem. Here the Williams (1986) and Linden and Kindermann (1989) (WLK) method has been used. This method uses the gradient descent as does the back-propagation algorithm (Linderman and Linden 1990). Given an initial $\mathbf{x}$, values are updated following

$$x_k^{i+1} = x_k^i - \eta \frac{\partial e}{\partial x_k^i}, \qquad (13)$$

where η is the back-propagation learning rate parameter, i is the iteration, x_k is the kth component of $\mathbf{x}$, and e is the error function. To the described net, we solve in reverse order

$$\frac{\partial e}{\partial x_k^i} = \delta_j, \qquad (14)$$

where the derivative delta δ_j is

$$\delta_j = \Psi(o_j)(o_j - o_j^*) \qquad (15)$$

if the neuron belongs to the output layer O, and

$$\delta_j = \Psi(o_j) \sum_{j \in H, O} \delta_j w_{j,m} \qquad (16)$$

if it belongs to the input layer I or the hidden one H.

In this work, a previous, more complex model was built, containing two more IR images, the 3×3 and 5×5 averages, and standard deviations for the eight IR images and the coldest pixels in the 5×5 window. The inversion procedures demonstrated the redundancy of these inputs in this particular case. Moreover, the 5×5 windows were interpreted as a source of noise in the training phase for a problem in which contradictory exemplars are common. Note that despite the high correlation between the 3×3 and 5×5 t_0 inputs (Table 3), these were judged necessary by the inversion algorithm.

A good example of the difficulties in rainfall merging techniques and the utility of using NN is the correlation estimation by using some models. As can be seen in Table 4, none of the analyzed models are capable of offering any significant correlation between the IR-derived inputs and rainfall measured by the SSM/I.

b. Histogram-matching technique description

The histogram-matching technique (Crosson et al. 1996) establishes a relationship between the probability density function (pdf) of the PMW rain rate and the IR brightness temperatures. The PMW rain-rate pdf is matched by accumulating the IR starting from the warm end and generating a series of matched pairs. After processing the past statistics as described, the time update cycle writes out a file that contains a lookup table for each selected box, which relates the IR temperature to the PMW rain rate. This file is then used to match the histograms of the following images, providing the rainfall rates. Figure 2 illustrates the procedure followed to generate the estimates using all the described procedures.

Before discussing the results obtained by applying the data fusion techniques to the proposed case study, we briefly recall the conventional IR technique used so far to estimate rainfall from space. We will use this algorithm for comparison with the proposed NN method.

c. GOES precipitation index algorithm

The GPI algorithm was first proposed using radar and satellite data collected during the Global Atmospheric Research Program Atlantic Tropical Experiment (Richards and Arkin 1981). It uses a fixed 235-K threshold temperature to distinguish between rain and no-rain pixels. First, the ratio between cloud pixels whose associated temperature is lower than 235 K and the number of total pixels in a given grid square is calculated. A constant rain rate (3 mm hr^{-1}) is then applied to the fraction of cold cloud to estimate the instantaneous rainfall, which can be then accumulated to monthly estimates. The rationale behind the method is to exploit the average relationship between low-temperature cloud-top pixels and rainfall. However, there is no direct relationship for any given pixel at any given time. The mismatch between cloud-top temperature and rainfall at

TABLE 3. Neural networks normalized inputs/output cross correlations at the 25-km spatial resolution for the 1800 UTC 12 Oct 2001 sample.

	T_b at t_0	T_b at t_1	T_b at t_2	T_b at t_3	T_b at t_4	T_b at t_5	T_b (3 × 3)	T_b (5 × 5)	∇T_b (3 × 3)	∇T_b (5 × 5)	#(T_b < 225)	PMW estimated rainfall
T_b at t_0	1	0.793	0.673	0.519	0.458	0.395	0.987	0.992	0.308	0.214	−0.689	−0.3
T_b at t_1	0.793	1	0.838	0.666	0.562	0.464	0.818	0.806	0.034	0.019	−0.568	−0.198
T_b at t_2	0.673	0.838	1	0.785	0.687	0.561	0.698	0.685	0.013	0.01	−0.476	−0.151
T_b at t_3	0.519	0.666	0.785	1	0.83	0.703	0.537	0.528	0.015	0.01	−0.31	−0.043
T_b at t_4	0.458	0.562	0.687	0.83	1	0.847	0.476	0.467	0.004	0.003	−0.262	−0.015
T_b at t_5	0.395	0.464	0.561	0.703	0.847	1	0.412	0.403	−0.011	−0.006	−0.202	0.048
T_b (3 × 3)	0.987	0.818	0.698	0.537	0.476	0.412	1	0.997	0.148	0.068	−0.7	−0.307
T_b (5 × 5)	0.992	0.806	0.685	0.528	0.467	0.403	0.997	1	0.198	0.09	−0.697	−0.304
∇T_b (3 × 3)	0.308	0.034	0.013	0.015	0.004	−0.011	0.148	0.198	1	0.897	−0.097	−0.033
∇T_b (5 × 5)	0.214	0.019	0.01	0.01	0.003	−0.006	0.068	0.09	0.897	1	−0.042	−0.018
#(T_b < 225)	−0.689	−0.568	−0.476	−0.31	−0.262	−0.202	−0.7	−0.697	−0.097	−0.042	1	0.305
Rainfall	−0.3	−0.198	−0.151	−0.043	−0.015	0.048	−0.307	−0.304	−0.033	−0.018	0.305	1

cloud base is partially corrected when large areas and time scales are considered.

4. Results and discussion

The results of the NN and histogram-matching techniques applied to a case study are shown in Fig. 3. The rain retrieval obtained applying the method described before on the SSM/I image was used together with the current and five previous IR images to generate the NN fusion retrieval. The HM estimate was created following the lookup table method and then has been resampled to the IR resolution. Since the GPI method can only provide binary rain–no-rain this not been mapped. The NN result clearly reflects better the SSM/I estimation so that, if the one obtained using only SSM/I is taken as an adequate rain-rate retrieval, the NN method seem to qualitatively improve over the HM rainfall estimation. The scatterplot of 30-min instantaneous estimates over an entire month (Fig. 4) demonstrates how dependent the HM and NN estimates are on the original PMW source, as expected. While the comparison with gauges leads to poorer correlations, the NN estimates appear to be related to the PMW measurements. Figure 4 also delimits the typical correlation values that can be expected from gauge–HM/NN comparison when a month of 30-min instantaneous data is chosen. By comparing these results with the 0.5°, 3-month accumulated values (in Fig. 10), the effects of spatial and temporal accumulation become apparent.

Figure 5 shows the relationship between the NN estimate and the SSM/I retrieval for a single case over the selected area. While the correlation coefficient of the SSM/I versus gauge data is similar to the earlier example, the advantage of the NN is that an estimate can be calculated every 30 min. The HM method is a straightforward, easy-to-calculate procedure that generates as good results for accumulated values as the GPI but generally performs worse than gauges when applied to instantaneous rainfall rates: correlation values of 0.19 against gauge (not shown) are far away from the correlation of 0.55 that the NN method provides (Fig. 5). An additional feature of the NN procedure is the increase in the spatial resolution of the retrieval in comparison with the IR resolution.

In principle, intercomparisons between different satellite-based procedures are subject to criticism as a unique validation method of assessment. For example, high correlations between the TRMM PR or ground radar and PMW cannot be taken as an absolute measurement of quality since both procedures are based on similar physical principles. Moreover, even if one of the comparison terms presents high correlation rates with the *real* rainfall values, transitivity cannot be applied: typically, high-confidence correlation values such as a 0.80 would yield a joint correlation of 0.64, not hard to achieve through Monte Carlo simulation. This would mean that independent ground-based measurements are

TABLE 4. Correlations of some classical models when comparing the T_b of the infrared image with interpolated gauge data (0.5° resolution) from Oct to Dec 2001.

Input	Method*	R^2	F	Sig f	Bound	a_0	a_1	a_2
T_b at t_0	LIN	0.09	636.72	0	0.4145	−0.3855		
	QUA	0.119	433.44	0	0.4179	−0.834	1.2534	
	CUB	0.137	340.69	0	0.4201	−1.4755	5.6351	−5.9588
	COM	0.096	685.53	0	0.4053	0.363		
	GRO	0.096	685.53	0	−0.9032	−1.0134		
	EXP	0.096	685.53	0	0.4053	−1.0134		
	LGS	0.093	655	0	1	1.4295	5.2305	

* LIN = linear; QUA = quadratic; CUB = cubic; COM = composite; GRO = grown; EXP = exponential; LGS = logistic.

required. On the other hand, checking against ground rain gauge measurements is not an absolute guarantee since gauge measurements have their own significant intrinsic uncertainties that have never been properly quantified (Smith et al. 1998).

A quantitative assessment of the results is conducted by comparing rain gauge measurements with instantaneous, daily, and monthly satellite retrievals based on fusion techniques. Several indices have been proposed for validation since Pearson's correlation does not properly reflect the performances of the satellite rainfall estimation methods. A review of some of the procedures is given by Cheng et al. (1993). The philosophy behind these indexes is to evaluate the method's ability to discriminate the rain boundary. Four measurements are produced that compare satellite estimate with rain gauge: rain–rain success (RR), rain/no-rain (RnR) errors, no-rain/rain (nRR) errors, and no-rain/no-rain (nRnR) agreement. With these four values, some indices can be generated:

PER (% error in the diagnosed area),

$$PER = \frac{nR - RnR}{nR + RR} \times 100; \qquad (17)$$

POD (probability of detection),

$$POD = \frac{RR}{RR + nRR}; \qquad (18)$$

FAR (false-alarm ratio),

$$FAR = \frac{RnR}{RnR + RR}; \qquad (19)$$

LFF (loss function F_i),

$$LFF = \frac{RnR}{RnR + RR} + \frac{nRR}{nRR + nRnR}; \qquad (20)$$

AWES (area-weighted error score),

$$AWES = \frac{RnR}{RnR + nRR} + \frac{nRR}{nRR + RR}; \quad \text{and} \quad (21)$$

SS (skill score),

$$SS = \frac{RR + nRnR - k}{RR + nRR + RnR + nRnR - k}, \qquad (22)$$

where

$$k = \frac{[(RR + nRR)(RR + RnR) + (RnR + nRnR)(nRR + nRnR)]}{RR + nRR + RnR + nRnR}. \qquad (23)$$

The meaning of most indexes can be derived easily from their arithmetical formulation. The skill score (SS) is particularly valuable since it relates the number of correct diagnoses with the expected correct number due to chance. It is also useful to notice that the results of all these indices are not related with the rainfall rate but with the rain/no-rain discrimination.

Table 5 shows the October and November 2001 statistics for the GPI, NN, and HM methods for 30-min estimates. The heading "% OCC" stands for percentage of occurrence, calculated as the percentage of the satellite estimate divided by the gauge measurement. Notice that gauge measurements are not interpolated in this

case, but are used as point estimates. In general, the results are poor as can be expected for almost instantaneous, noninterpolated estimates. However, the indices support the idea that, in term of scores, the NN method is at least comparable to the HM and PMW estimation procedures. Unsurprising, the binary threshold of the GPI works well in delimiting the rainfall boundaries and even the rainfall amount but cannot be considered as a realistic estimate for these short-term, high-resolution scales.

Another method of evaluating the performances of the estimates is by comparing their histograms. Figure 6 shows a monthly histogram for coincident points.
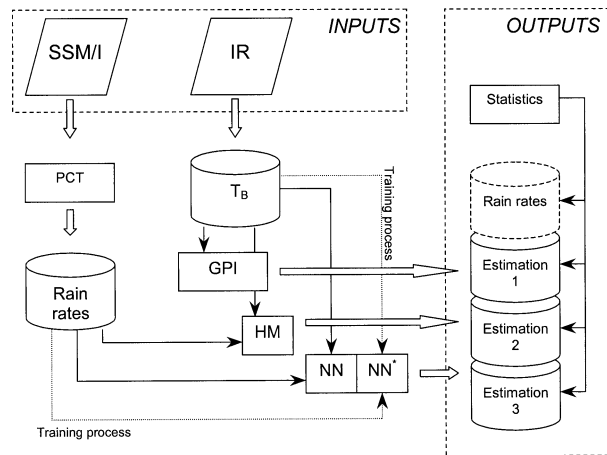
FIG. 2. Flow diagram of the processes followed to generate the rainfall rates using the GPI, HM, and NN methods from satellite information.

The NN estimates seem to improve in this case the results over the other methods: the NN histogram closely follows the gauge one, while the HM and PMW lines present more differences with the gauge reference value.

The real added value of the fusion procedures is to provide a PMW-based rainfall estimate when only IR information is available as illustrated in Fig. 7. Using a single image to calibrate the NN, the whole temporal evolution of the rainfall system can be followed at the IR spatial resolution. The spatial and temporal resolutions of the NN results allow the analysis of the life cycle of rainfall systems to a scale as small as permitted by the IR image resolution. The typical development of a front and small convective cells can be tracked at 30-min intervals. This has proved to be useful, both for case study analysis and for agricultural and hydrological applications. A forthcoming application of this method to MSG images will generate ~5 km, 15-min rainfall estimation at the geostationary scale. It is, however, debatable whether these estimates reflect the real behavior of the rain fields (cf. Fig. 8). Nevertheless, since it is widely accepted that PMW sensors provide the most direct estimates of global rainfall currently available (e.g., Todd et al. 2001) the effectiveness of the NN method both at instantaneous and accumulated time scales depends ultimately on the SSM/I estimate. Once it is accepted that the SSM/I sensors accurately measure the rainfall, our results show that the fused NN method is able to *simulate* correctly the PMW estimate.

The time series of rainfall events (Fig. 8) shows how sparse the PMW estimates are compared with the fused HM and NN methods. This improvement in the temporal resolution is the main advantage of the NN approach over the direct PMW measurements since the scores of these methods are somehow similar (see Table 5). On the other hand, the main advantage over the HM is the

increase in the spatial resolution, since the NN is able to weight the IR contributions to a single PMW pixel, thus generating subpixel rainfall estimates. Therefore, using IR imagery makes it possible to extend the PMW capabilities avoiding to some extent the *snapshot* character of the SSM/I observations while also increasing the spatial resolution. However, the estimates are by the nature of the NN training data, representative of a microwave gridbox-sized area average.

Figure 8 plots 30-min series over a complete day for four locations across Andalusia. Although the three methods reflect to some extent the temporal variations, the absolute values are not accurately estimated. Some authors (Bellerby et al. 2000) have reported similar conclusions that may be due to problems affecting the SSM/I rainfall estimation. First, the SSM/I scan can only provide snapshot observations of the actual weather system that will be eventually transformed into rainfall rates. However, rainfall inhomogeneities are well known and it is possible that a station recording no rain during the SSM/I overpass may measure a high-rainfall amount a few minutes later. Careful choice of gauge locations in places representative of the neighboring area would not be enough to solve this problem. Some ''delay'' effects in Fig. 8 could be attributable to this effect. Another even more important problem is that SSM/I retrieves the integral rainfall along the entire atmospheric column while the gauge only measures surface rainfall. Evaporating rainfall could be one of the reasons of the overestimation that is identifiable in Fig. 5. The scores (Table 5) are also affected as the no-rain/rain score increases. Needless to say that the correct quantitative assessment of this water amount is crucial for meteorological and forecasting purposes. New strategies are currently being conceived to adequately address the calibration–validation issue for satellite rainfall algorithms. These strategies have to go a step ahead in facing the problems of the microphysics of the rain processes together with the answers to be given to the end users for the assimilation of rain rates into weather, climate, and hydrological prediction models (Smith et al. 2002). Nonetheless, validation procedures by means of independent ground-based measurements will continue to be needed, if nothing else as a basis for research on new validation methodologies.

This leads us to suggest that rainfall gauge measurements are probably not the optimum way to validate *instantaneous* SSM/I estimates in so far that they measure different parameters related with rainfall. The 30-min gauge integration time would be too large to take account of the earlier-mentioned effects. However, their effects may be mitigated to a certain extent by area and time accumulations allowing for a quantitative validation of the estimates.

In order to demonstrate the expected improvement when dealing with accumulated values, we compared the NN estimates with the gauge measurements. The

SSM/I retrieval

12 10 01 @ 18 00
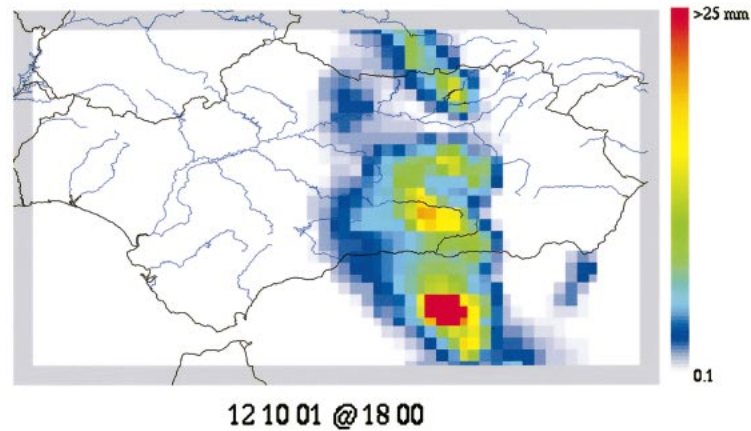
Neural Network fusion

12 10 01 @ 18 00

Histogram Matching result

12 10 01 @ 18 00
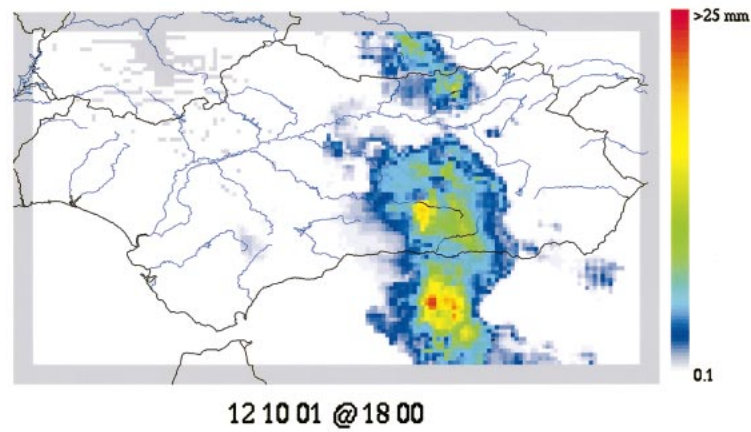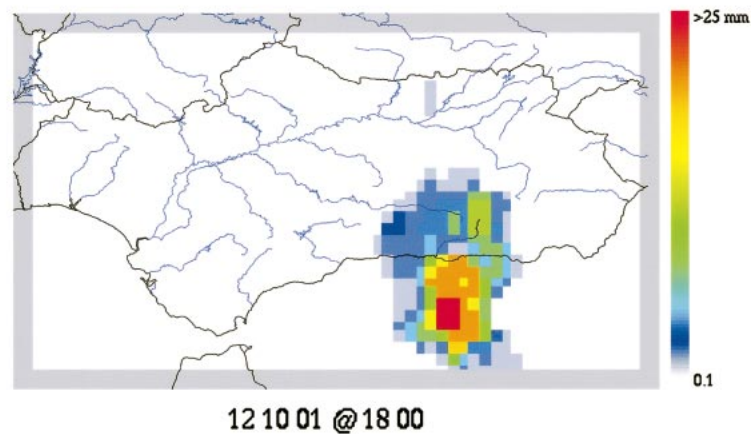
FIG. 3. Single-image comparison between resampled 0.1° rain retrieval from (top) the SSM/I using PCT (Kidd 1998), (middle) ~0.05° NN estimate, and (bottom) 0.1° HM estimate. Time/date is 1800 UTC 12 Oct 2001.
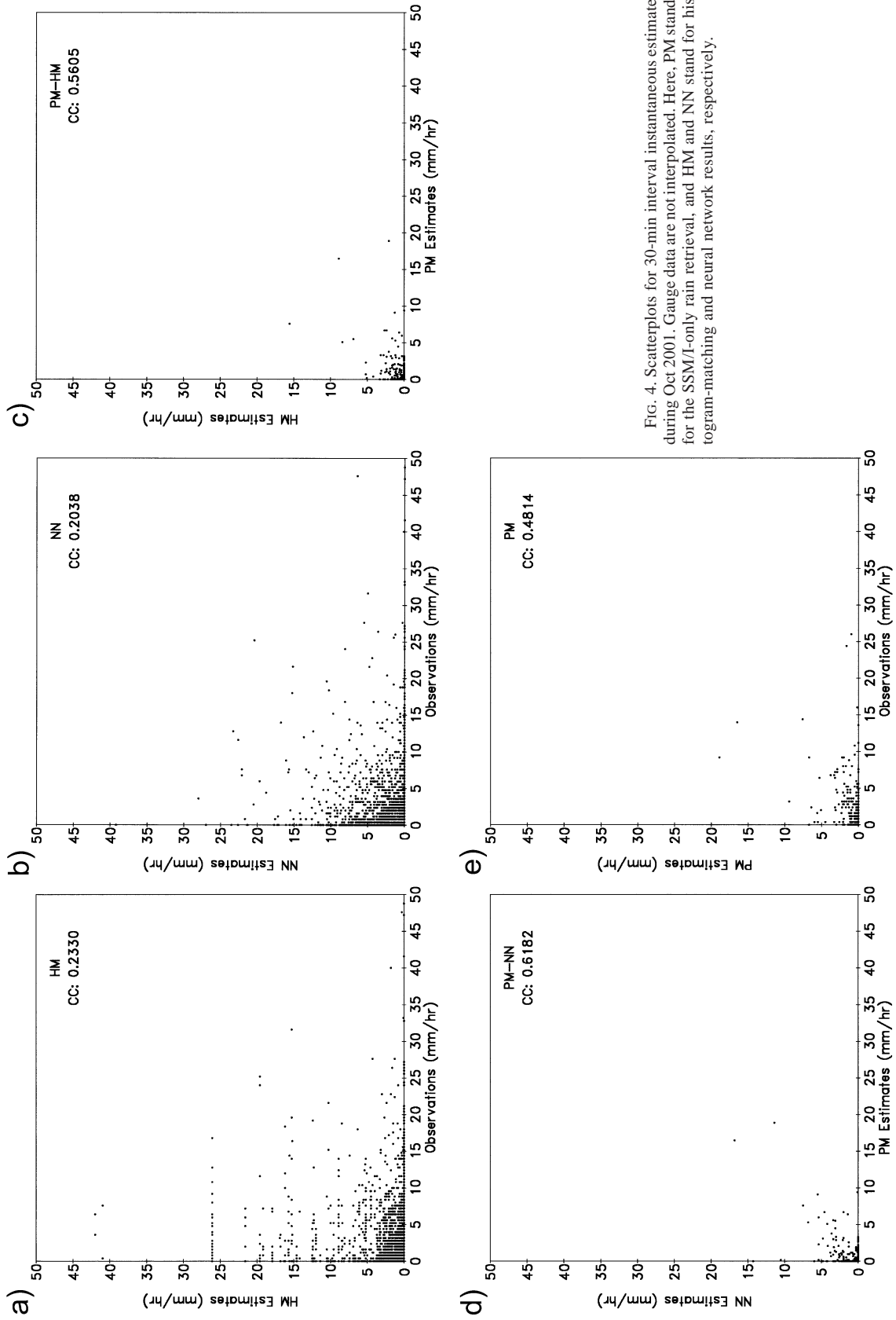
FIG. 4. Scatterplots for 30-min interval instantaneous estimates during Oct 2001. Gauge data are not interpolated. Here, PM stands for the SSM/I-only rain retrieval, and HM and NN stand for histogram-matching and neural network results, respectively.

a)

b)

c)
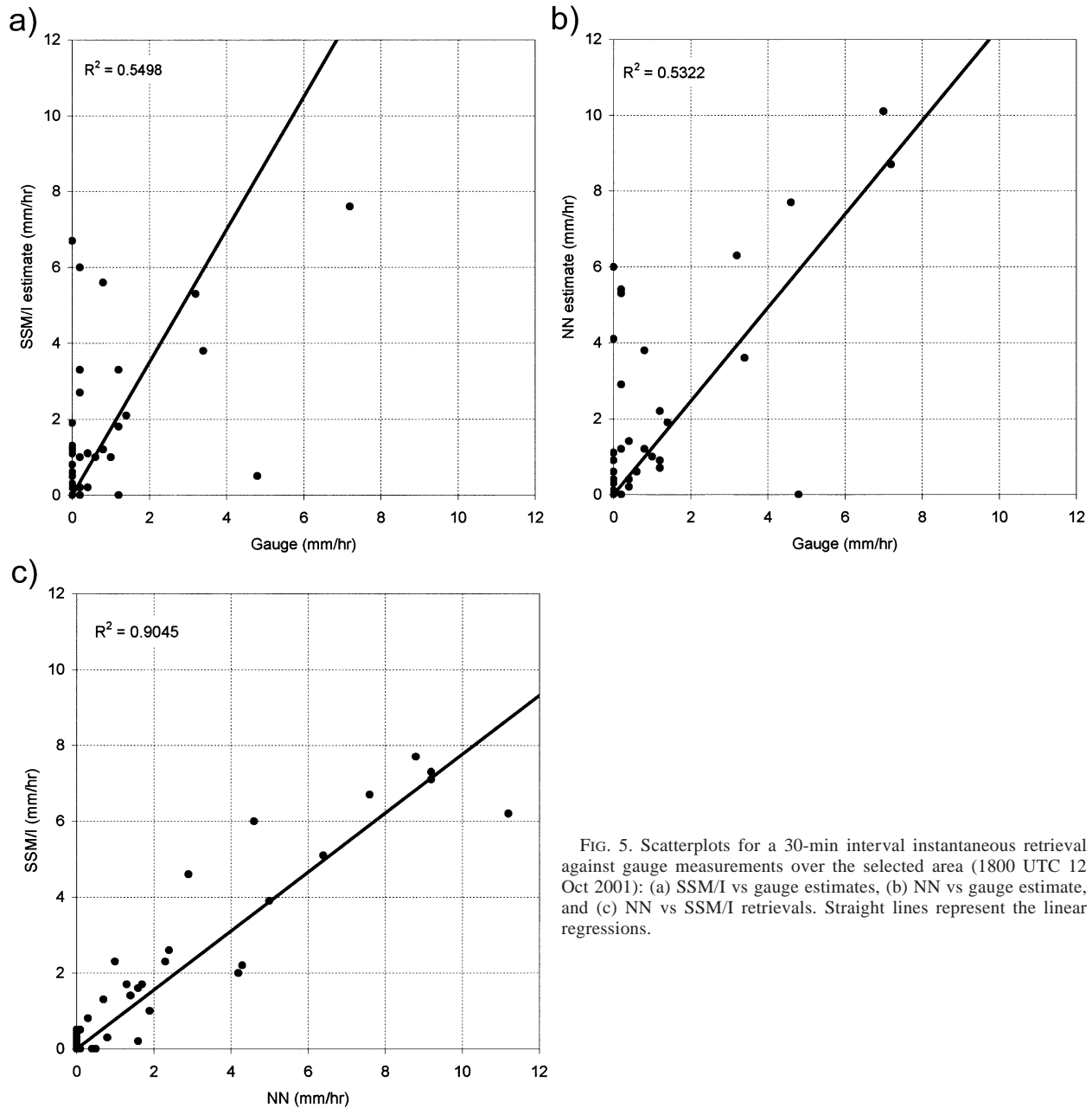
FIG. 5. Scatterplots for a 30-min interval instantaneous retrieval against gauge measurements over the selected area (1800 UTC 12 Oct 2001): (a) SSM/I vs gauge estimates, (b) NN vs gauge estimate, and (c) NN vs SSM/I retrievals. Straight lines represent the linear regressions.

maximum entropy method was used to interpolate the gauge stations measurements to $0.1° × 0.1°$ and $0.5° × 0.5°$ boxes providing areal estimates, as discussed above. Figure 9 shows that the correlation coefficient improves for a $0.1° × 0.1°$ resampling area, a large number (October 2001) of 30-min estimations, and a selection of those gauge locations with at least one PMW value during the period. Moreover, if the subset of those cells that contain more than four gauge stations is selected and the resolution reduced to $0.5° × 0.5°$, the R^2 value increases notably (Fig. 10). As expected, the downscaling of the whole dataset to $0.5° × 0.5°$

cells also increases the correlation as shown in Fig. 11. This is in accordance with similar values reported in the literature for accumulated values using different methods of those shown here, but it is worth noting that the original values and correlations are only truly represented in Fig. 4. Using no artifices to encompass the biases, current satellite rainfall estimates can only provide limited accuracies for short time and spatial scales. Turk et al. (2002) have demonstrated how a reliable methodology can provide 0.8 R^2 values for $2.5° × 2.5°$, monthly estimates and apparently poor values such as 0.tbR^2 for $0.2° × 0.2°$, 90-min estimates. In that work

TABLE 5. Statistics for the GPI, HM, and NN fusion methods from 1 Oct to 30 Nov 2001. Results are compared with point gauge measurements. Here, nRnR stands for no rain in the estimate and no rain in gauge.

	Bias	Ratio	Rmse	R^2	No.	nRnR	nRR	RnR	RR	POD	FAR	AWES	SS	%OCC	PER	LFF
Oct 2001																
NN	−0.05	0.51	1.82	0.12	115 934	109 093	2074	3643	1124	0.24	0.65	0.68	0.26	67	−49.06	0.78
HM	−0.06	0.47	0.87	0.163	122 649	115 943	1978	3760	968	0.20	0.67	0.70	0.23	62	−60.49	0.81
GPI	0	1.01	0.65	0.364	121 219	113 818	2830	2790	1781	0.39	0.61	0.64	0.36	101	0.87	0.63
PMW	−0.07	0.4	0.68	0.161	14 479	13 640	313	426	100	0.19	0.76	0.79	0.19	79	−27.36	0.83
Nov 2001																
NN	−0.06	0.37	1.36	0.142	230 705	218 006	2869	8291	1539	0.16	0.65	0.69	0.19	45	−123.00	0.86
HM	−0.06	0.34	0.71	0.137	241 366	230 297	3310	6368	1391	0.18	0.70	0.73	0.20	61	−65.05	0.83
GPI	0	1	0.62	0.311	239 092	226 514	5041	5024	2513	0.33	0.67	0.69	0.31	100	0.23	0.69
PMW	−0.06	0.36	0.6	0.123	30 012	27 958	1118	771	165	0.18	0.87	0.90	0.12	137	27.05	0.86
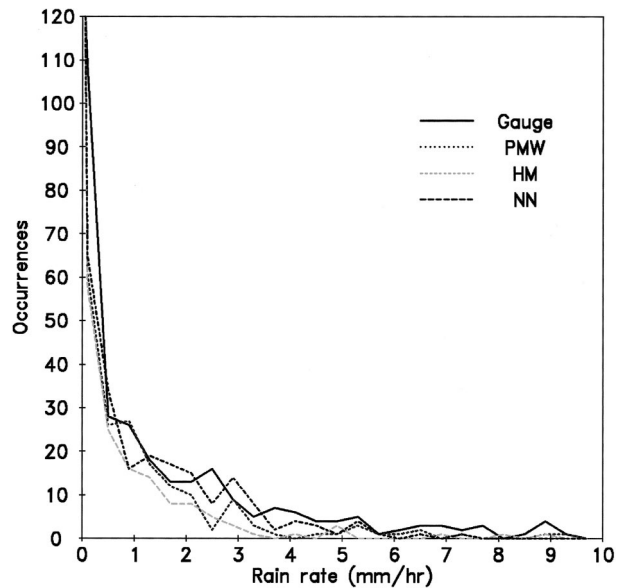
FIG. 6. Histogram of monthly estimation (Oct 2001) for coincident gauge data, PMW measurement, and HM and NN estimations.

correlations of 0.6 can be achieved by coarsening the spatial resolution to $1.5° \times 1.5°$ over a 3-h analysis, which gives an idea of the variations in the results that can be expected.

5. Conclusions

Rainfall at midlatitudes is spatially and temporally very different from tropical rainfall. Processes that favor rainfall estimates such as the daily cycle are substituted by more complex mechanisms that are not easy to model. This represents a challenge both to rainfall estimation and to the validation of the results.

Instantaneous rainfall retrieval through PMW sensors presents many advantages over the IR-based techniques or over gauges, but disadvantages such as the temporal sampling and the spatial resolution must be also considered. Data fusion and merging approaches using IR information are capable of mitigating these drawbacks without removing the physically based rainfall discrimination they provide. Some methods, such as the NNs even improve the results of the PMW sensors themselves in terms of spatial resolution.

Validation procedures based on spatial interpolation generate smooth surfaces that encompass the patchy nature of rain and the satellite update time. Time-accumulated values deal with the latter issue and also with the climatic temporal series convergence property for large values. Despite the problems, accumulated values are valuable for intercomparison purposes.

A neural network–based PMW–IR satellite merging method relies upon the careful design of the net, which is based on the nature of the data and provides a repeatable, analytical, objective process. The resulting net

12 10 01 @ 17 00

12 10 01 @ 17 30

12 10 01 @ 18 00

12 10 01 @ 18 30

>25 mm

12 10 01 @ 19 00

12 10 01 @ 19 30

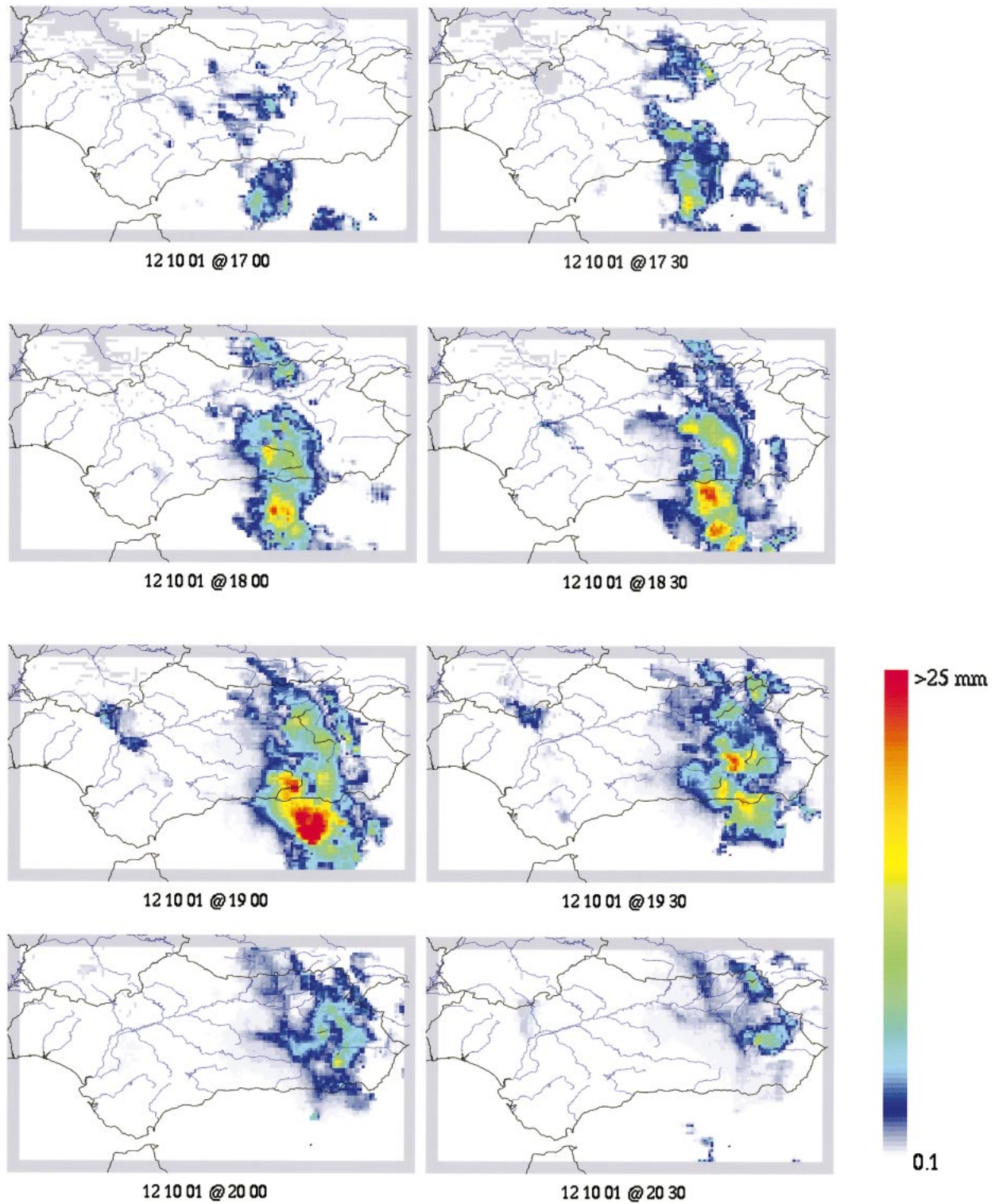0.1

12 10 01 @ 20 00

12 10 01 @ 20 30

FIG. 7. Example of instantaneous NN-derived rainfall evolution. The neural net was trained once at 1800 UTC (left, second row) and then applied forward and backward to generate the estimates using IR information only.
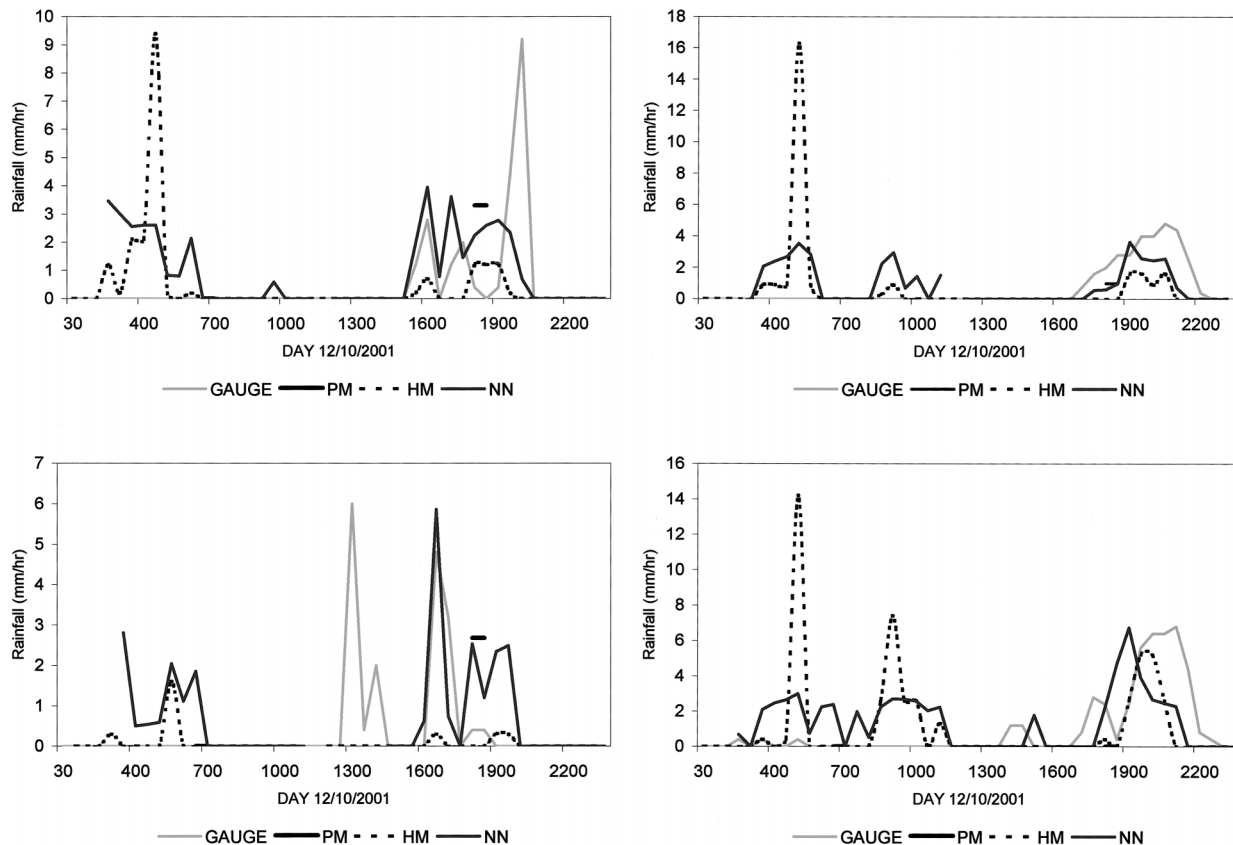
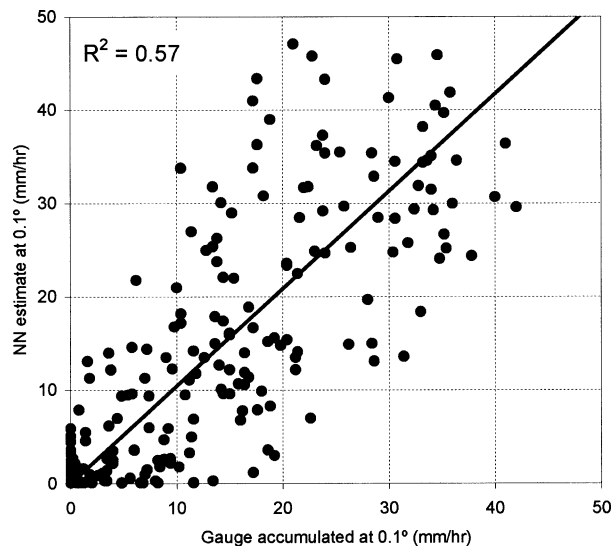FIG. 8. Time series of instantaneous rainfall estimations for four different gauge point locations randomly selected (and unspecified).

FIG. 9. Scatterplot comparison between instantaneous rainfall estimation using the NN method and gauge measurements at $0.1° \times 0.1°$ during the best case analysis (Oct 2001) for coincident PMW points.

has been compared with other models and paradigms, proving comparable performances in terms of rain delimitation scores and an increase in the temporal and spatial resolutions. Its rainfall retrieval capabilities have been tested against GPI, HM, and gauge data—improving the temporal resolution of the PMW estimates and providing reasonable discrimination capabilities. Average correlation values of 0.6 for $0.1° \times 0.1°$ and 0.7 for $0.5° \times 0.5°$ monthly accumulated values are obtained, with possible correlation values of up to 0.8 for those areas that participate in the training process. The temporal rainfall variability over a location is recognized by the NN as the life cycle of the rainfall processes too. Further advances are expected from ongoing work on the subject. The forthcoming use of MSG images could improve the match between IR and PMW images, and instantaneous validation procedures are being developed to avoid the snapshot effect of the SSM/I imagery and to establish a relationship between its estimations and time series accumulated values.

However, a huge advance on rainfall estimates can only be expected if the PMW measurement technology improves. Combined, fused algorithms ultimately rely on the PMW discrimination capacity and on the IR temporal sampling and spatial definition capabilities. The IR information such as those provided by the MSG
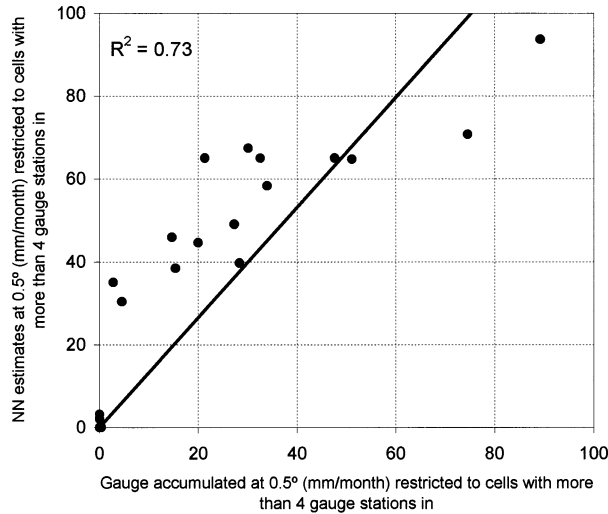
FIG. 10. Scatterplot comparison between point estimates at 0.5° × 0.5° resolution and the NN results restricted to cells with more than four gauge stations.

channels are ready to offer reasonable performances at these wavelengths. While it is clear that the PMW approach is the best paradigm to generate accurate rainfall estimates, technical problems remain. The Algorithm Intercomparison Projects (AIP) (Smith et al. 1998) and many research papers have identified limitations that future PMW-based missions need to address if a great advance in rainfall estimation is to result. High correlations of satellite rainfall estimates are linked with a selection of spatially interpolated (typically at 0.5°) and temporal accumulated values (typically monthly). Less than 1° resolution and hourly estimates currently provide very low correlations and can only be enhanced by improving the PMW capabilities since combined, fused
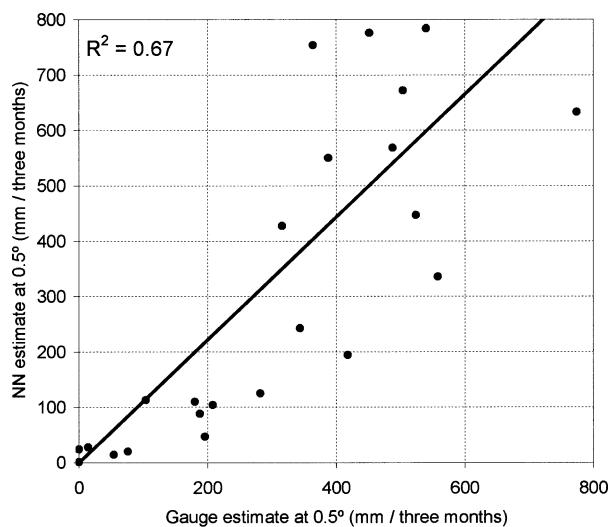

FIG. 11. Scatterplot comparison between measured accumulated rainfall during Oct, Nov, and Dec 2001 at 0.5° × 0.5° resolution and the NN performances.

methodologies' performances are linked with this essential source of rainfall information.

REFERENCES

Adler, R. F., A. J. Negri, P. R. Keehn, and I. M. Hakkarinen, 1993: Estimation of monthly rainfall over Japan and surrounding waters from a combination of low-orbit microwave and geosynchronous IR data. *J. Appl. Meteor.,* **32,** 335–356.

Anagnostou, E. N., A. J. Negri, and R. F. Adler, 1999: A satellite infrared technique for diurnal rainfall variability studies. *J. Geophys. Res.,* **104** (D24), 31 477–31 488.

Anders, U., and O. Korn, 1999: Model selection in neural networks. *Neural Networks,* **12,** 309–323.

Bellerby, T., M. Todd, D. Kniveton, and C. Kidd, 2000: Rainfall estimation from a combination of TRMM precipitation radar and GOES multispectral satellite imagery through the use of an artificial neural network. *J. Appl. Meteor.,* **39,** 2115–2128.

Carpenter, G. A., S. Grossberg, and S. Mehanian, 1989: Invariant recognition of cluttered scenes by a self-organizing ART architecture: CORT-X boundary segmentation. *Neural Networks,* **2,** 1169–1181.

——, M. N. Gjaja, S. Gopal, and C. E. Woodcock, 1997: ART neural networks for remote sensing: Vegetation classification from Landsat TM and terrain data. *IEEE Trans. Geosci. Remote Sens.,* **35,** 308–325.

Cheng, M., R. Brown, and C. G. Collier, 1993: Delineation of precipitation areas using Meteosat infrared and visible data in the region of the United Kingdom. *J. Appl. Meteor.,* **32,** 884–898.

Christakos, G., 1991: Some applications of the Bayesian maximum-entropy concepts in geostatistics. *Maximum Entropy and Bayesian Methods,* W. T. Grandy and L. H. Schick, Eds., Kluwer, 215–229.

Crosson, W. L., C. E. Duchon, R. Raghavan, and S. J. Goodman, 1996: Assessment of rainfall estimates using a standard Z–R relationship and the probability matching method applied to composite radar data in central Florida. *J. Appl. Meteor.,* **35,** 1203–1219.

Cybenko, G., 1989: Approximation by superposition of a sigmoidal function. *Math. Control Signals Syst.,* **2,** 303–314.

Dagher, I., M. Georgiopoulos, G. L. Heileman, and G. Bebis, 1999: An ordering algorithm for pattern presentation in fuzzy ART-MAP that tends to improve generalization performance. *IEEE Trans. Neural Networks,* **10,** 768–779.

Ebert, E. E., 1996: Results of the 3rd Algorithm Intercomparison Project (AIP-3) of the Global Precipitation Climatology Project

(GPCP). BMRC Rep. 55, Bureau of Meteorology Research Centre.

Ferraro, R. R., 1997: SSM/I derived global rainfall estimates for climatological applications. *J. Geophys. Res.,* **102,** 16 715–16 735.

Grossberg, S., 1969: Some networks that can learn, remember and reproduce any number of complicated space-time patterns. *J. Math. Mech.,* **19,** 53–91.

Herman, A., V. Kumar, P. Arkin, and J. Kousky, 1997: Objectively determined 10-day African rainfall estimates created for famine early warning systems. *Int. J. Remote Sens.,* **18,** 2147–2159.

Hornik, K., M. Stinchcombe, and H. White, 1989: Multilayer neural networks are universal approximators. *Neural Networks,* **2,** 359–366.

Hsu, L., H. V. Gupta, X. Gao, and S. Sorooshian, 1999: Estimation of physical variables from multi-channel remotely sensed imagery using a neural network: Application to rainfall estimation. *Water Resour. Res.,* **35,** 1605–1618.

Janowiak, J. E., R. J. Joyce, and Y. Yarosh, 2001: A real-time global half-hourly pixel-resolution infrared dataset and its applications. *Bull. Amer. Meteor. Soc.,* **82,** 205–217.

Jaynes, E. T., 1963: Information theory and statistical mechanics. *Statistical Physics,* K. Ford Ed., Benjamin.

——, 1990: Probability theory as logic. *Maximum-Entropy and Bayesian Methods,* P. F. Fougère, Ed., Kluwer.

Jensen, C. A., R. D. Reed, R. J. Marks II, M. A. El-Sharkawi, J.-B. Jung, R. T. Miyamoto, G. M. Anderson, and C. J. Eggen, 1999: Inversion of feedforward neural networks: Algorithms and applications. *Proc. IEEE,* **87,** 1536–1549.

Kapur, J. N., and H. K. Kesavan, 1992: *Entropy Optimization Principles with Applications.* MIT Academic Press, 408 pp.

Kidd, C., 1998: On rainfall retrieval using polarization-corrected temperatures. *Int. J. Remote Sens.,* **19,** 981–996.

Kummerow, C., and L. Giglio, 1995: A method for combining passive microwave and infrared rainfall observations. *J. Atmos. Oceanic Technol.,* **12,** 33–45.

Lee, Y. M., 1998: A methodological study of the application of the maximum entropy estimator to spatial interpolation. *J. Geoor. Inf. Decis. Anal.,* **2,** 265–276.

——, and J. H. Ellis, 1997: Estimation and simulation of lognormal random fields. *Comput. Geosci.,* **23,** 19–31.

Levizzani, V., J. Schmetz, H. J. Lutz, J. Kerkmann, P. P. Alberoni, and M. Cervino, 2001: Precipitation estimations from geostationary orbit and prospects for METEOSAT Second Generation. *Meteor. Appl.,* **8,** 23–41.

Li, L., J. Vivekanandan, C. H. Chan, and L. Tsang, 1997a: Microwave radiometric technique to retrieve vapor, liquid and ice. Part I-Development of a neural network-based inversion method. *IEEE Trans. Geosci. Remote Sens.,* **35,** 224–236.

——, ——, ——, and ——, 1997b: Microwave radiometric technique to retrieve vapor, liquid and ice. Part II- Joint studies of radiometer and radar winter clouds. *IEEE Trans. Geosci. Remote Sens.,* **35,** 237–247.

Linden, A., and J. Kindermann, 1989: Inversion of multilayer nets. *Proc. Int. Joint. Conf. Neural Networks,* Vol. II, San Diego, CA, IEEE, 425–430.

Linderman, J., and A. Linden, 1990: Inversion of neural networks by gradient descent. *Parallel Comput.,* **14,** 277–286.

Marzano, F. S., A. Mugnai, G. Panegrossi, N. Pierdicca, E. A. Smith, and J. Turk, 1999: Bayesian estimation of precipitating cloud parameters from combined measurements of spaceborne microwave radiometer and radar. *IEEE Trans. Geosci. Remote Sens.,* **37,** 596–613.

——, M. Palmacci, D. Cimini, and J. F. Turk, 2002: Statistical integration of satellite passive microwave and infrared data for high-temporal sampling retrieval of rainfall. *Proc. IGARSS'02,* Toronto, Canada, IEEE.

Murata, N., S. Yoshizawa, and S. Amari, 1994: A criterion for determining the number of parameters in an artificial neural network model. *IEEE Trans. Neural Networks,* **5,** 865–872.

Noll, D., 1997: Restoration of degraded images with maximum entropy. *J. Global Optimization,* **10,** 91–103.

Richards, F., and P. Arkin, 1981: On the relationship between satellite-observed cloud cover and precipitation. *Mon. Wea. Rev.,* **109,** 1081–1093.

Sarle, W. S., 1994: Neural networks and statistical models. *Proc. 19th Annual SAS Users Group International Conference,* Cary, NC, SAS Institute, 1538–1550.

Schmetz, J., P. Pili, S. Tjemkes, D. Just, J. Kerkmann, S. Rota, and A. Ratier, 2002: An introduction to Meteosat Second Generation (MSG). *Bull. Amer. Meteor. Soc.,* **83,** 977–992.

Shannon, C. E., 1948: A mathematical theory of the communication. *Bell Syst. Tech. J.,* **27,** 379–423.

Shore, J. E., and R. W. Johnson, 1980: Axiomatic derivation of the principle of maximum entropy and the principle of minumum cross-entropy. *IEEE Tran. Inf. Theory,* **26,** 26–39.

Sivapalan, M., and G. Blöschl, 1998: Transformation of point rainfall to areal rainfall: Intensity–duration–frequency curves. *J. Hydrol.,* **204,** 150–167.

Skilling, J., and R. K. Bryan, 1984: Maximum entropy image reconstruction: General algorithm. *Mon. Not. Roy. Astron. Soc.,* **211,** 111–124.

Smith, D. M., D. R. Kniveton, and E. C. Barrett, 1998: A statistical modeling approach to passive microwave rainfall retrieval. *J. Appl. Meteor.,* **37,** 135–154.

Smith, E. A., and Coauthors, 1998: Results of WetNet PIP-2 project. *J. Atmos. Sci.,* **55,** 1483–1536.

——, and Coauthors, 2002: Precipitation retrieval: Algorithm and calval architecture. GPM Science Implementation Plan.

Sorooshian, S., K. L. Hsu, X. Gao, H. V. Gupta, B. Imam, and D. Braithwaite, 2000: Evaluation of PERSIANN system satellite-based estimates of tropical rainfall. *Bull. Amer. Meteor. Soc.,* **81,** 2035–2046.

Tapiador, F. J., and J. L. Casanova, 2002: An algorithm for the fusion of images based on Jaynes' maximum entropy method. *Int. J. Remote Sens.,* **23,** 777–786.

Todd, M. C., and R. Washington, 1999: A simple method to retrieve 3-hourly estimates of global tropical and subtropical precipitation from International Satellite Cloud Climatology Program (ISCCP) D1 data. *J. Atmos. Oceanic Technol.,* **16,** 146–155.

——, E. C. Barrett, M. J. Beaumont, and J. Green, 1995: Satellite identification of rain days over the upper Nile River basin using an optimum infrared rain/no-rain threshold temperature model. *J. Appl. Meteor.,* **34,** 2600–2611.

——, C. Kidd, D. Kniveton, and T. J. Bellerby, 2001: A combined satellite infrared and passive microwave technique for estimation of small-scale rainfall. *J. Atmos. Oceanic Technol.,* **18,** 742–755.

Turk, F. J., G. D. Rohaly, J. Hawkins, E. A. Smith, F. S. Marzano, A. Mugnai, and V. Levizzani, 1999: Meteorological applications of precipitation estimation from combined SSM/I, TRMM and infrared geostationary satellite data. *Microwave Radiometry and Remote Sensing of the Earth's Surface and Atmosphere,* P. Pampaloni and S. Paloscia, Eds., VSP Int. Science Publishers, 353–363.

——, E. E. Ebert, H.-J. Oh, and B.-J. Sohn, 2002: Validation and applications of a realtime global precipitation analysis. *Proc. IGARSS,* Toronto, Canada, IEEE.

Vicente, G., R. A. Scofield, and W. P. Menzel, 1998: The operational GOES infrared rainfall estimation technique. *Bull. Amer. Meteor. Soc.,* **79,** 1883–1898.

Williams, R. J., 1986: Inverting a connectionist network mapping by backpropagation of error. *Proc. 8th Annual Conf. of the Cognitive Science Society,* Hillsdale, NJ, Cognitive Science Society, 859–865.

Xu, L., X. Gao, S. Sorooshian, and P. A. Arkin, 1999: A microwave infrared threshold technique to improve the GOES precipitation index. *J. Appl. Meteor.,* **38,** 569–579.